



This is a repository copy of *Modelling the nucleation, growth and coarsening kinetics of γ (D0₂₂) precipitates in the Ni-base Alloy 625.*

White Rose Research Online URL for this paper:
<http://eprints.whiterose.ac.uk/104401/>

Version: Accepted Version

Article:

Moore, I.J., Burke, M.G. and Palmiere, E.J. orcid.org/0000-0002-4048-8536 (2016)
Modelling the nucleation, growth and coarsening kinetics of γ (D0₂₂) precipitates in the Ni-base Alloy 625. *Acta Materialia*, 119. pp. 157-166.
ISSN 1359-6454

<https://doi.org/10.1016/j.actamat.2016.08.027>

Reuse

This article is distributed under the terms of the Creative Commons Attribution-NonCommercial-NoDerivs (CC BY-NC-ND) licence. This licence only allows you to download this work and share it with others as long as you credit the authors, but you can't change the article in any way or use it commercially. More information and the full terms of the licence here: <https://creativecommons.org/licenses/>

Takedown

If you consider content in White Rose Research Online to be in breach of UK law, please notify us by emailing eprints@whiterose.ac.uk including the URL of the record and the reason for the withdrawal request.



eprints@whiterose.ac.uk
<https://eprints.whiterose.ac.uk/>

Modelling the nucleation, growth and coarsening kinetics of γ'' (D0₂₂) precipitates in the Ni-Base Alloy 625

I. J. Moore^{a,*}, M. G. Burke^b, E. J. Palmiere^a

^a*Department of Materials Science and Engineering, The University of Sheffield, Sir Robert Hadfield Building, Mappin Street, Sheffield, S1 3JD, UK.*

^b*Materials Performance Centre, The University of Manchester, The Mill, Sackville Street, Manchester, M13 9PL, UK.*

Abstract

Alloy 625 is susceptible to significant precipitation hardening through the formation of γ'' (D0₂₂-NbNi₃) particles. These precipitates can form both during manufacture and in high temperature service and, consequently, the accurate prediction of their behaviour is crucial. To this end, a model is presented here which describes γ'' precipitation in Alloy 625, encompassing the concurrent nucleation, growth and coarsening of different particles and allowing for the particles to be shape changing. This model is calibrated with respect to the experimentally measured aspect ratio evolution observed at 650°C. The resultant outputs for interfacial energy, particle size distribution and number density are in agreement with experimental data for a simulation of 1000 hours at 650°C.

Keywords:

Modelling, Precipitation Kinetics, Coarsening, Nickel based alloys, γ''

1. Introduction

Thanks to its excellent corrosion resistance and strength at elevated temperatures, Alloy 625 is widely utilised in a number of industries such as chemical processing, automotive transportation and marine oil extraction [1, 2, 3, 4, 5, 6]. Furthermore, the alloy also exhibits

*Corresponding author

Email address: imoore1@sheffield.ac.uk (I. J. Moore)

5 good resistance to irradiation assisted stress corrosion cracking [7] and the combination of these properties have led to it becoming a candidate material for selected current and future nuclear applications. The precipitation of $\text{Ni}_3\text{Nb}(\text{Al},\text{Ti})$ γ'' particles (body-centre-tetragonal (BCT) unit cell corresponding to Figure 1 and orientation relationship $[001]_{\gamma''} \parallel \langle 100 \rangle_{\gamma}$) can lead to significant hardening of the superalloy through the formation of coherency strains
 10 [8], with the degree imparted strongly dependent on the precipitate size [9] and density [10]. Consequently, the ability to predict the evolution of these latter variables is key to accurate material thermomechanical processing and assessment in service.

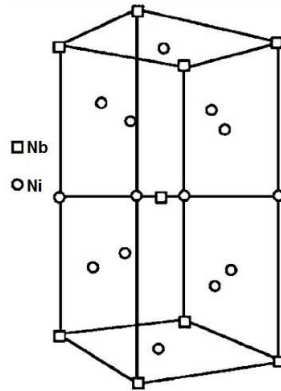


Figure 1: BCT $D0_{22}$ unit cell of γ'' ($\text{Ni}_3\text{Nb}(\text{Al},\text{Ti})$), adapted from [11].

In contrast to many established modelling techniques the relatively recently developed SFFK (Svoboda-Fischer-Fratzl-Kozeschnik) model, derived using the Onsager thermodynamic extremum principle, provides considerable flexibility both in terms of precipitate
 15 shape and alloy composition [12, 13, 14]. Resultantly, owing to the oblate spheroidal shape of γ'' particles and the large number of alloying elements in Alloy 625, it is using the SFFK framework that the model outlined in this research is developed.

2. Model Description

20 Like other numerical mesoscale precipitation models, such as that developed by Kampmann and Wagner (KW) [15, 16], the SFFK model is a class computation [17] in which

the evolution of groups (or classes) of particles, each retaining the same physical properties such and size and shape, is calculated rather than that of individual precipitates to achieve the highest computational efficiency whilst retaining appropriate detail [18]. However unlike classical approaches such as KW, the removal of some details in the SFFK model, specifically the lack of concentration profiles means that it can be much more easily applied to large/many component systems saving significant computation time. That is to say, although the KW method, specifically the equations governing precipitate evolution, can theoretically be applied to complex systems, substantial numerical difficulties are incurred (particularly associated with coupling conditions across the precipitate matrix interface) when modelling systems with component numbers equivalent to those of Alloy 625. By using a mean field approach the SFFK model avoids this problem [19].

2.1. Nucleation

Nucleation is calculated in the present model according to classical nucleation theory: Defining \dot{N} as the nucleation rate per unit volume, N_0 as the nucleation site density, β^* as the atomic absorption rate, τ as the incubation time, t as the time, k_B as the Boltzmann constant, T as the temperature in kelvin, ΔG^* as the activation energy required for nucleation and Z as the Zeldovich factor, the governing expression becomes Equation 1 [20, 21, 22, 23, 24, 25, 26]. In this instance, the Zeldovich factor and incubation time are determined according to Equation 2 (where $\Delta G(n)$ is the free energy of forming a microcluster containing n atoms) and Equation 3, respectively.

$$\dot{N} = N_0 Z \beta^* \exp\left(\frac{-\Delta G^*}{k_B T}\right) \exp\left(\frac{-\tau}{t}\right) \quad (1)$$

$$Z = -\sqrt{\frac{1}{2\pi k_B T} \left(\frac{\partial^2 \Delta G(n)}{\partial n^2}\right)_{n^*}} \quad (2)$$

$$\tau = \frac{1}{2Z^2\beta^*} \quad (3)$$

Ignoring diffusion inside the precipitate (and *ipso facto* any variation chemical composition), the value for the atomic impingement rate is found according to Equation 4 in which ρ^* corresponds to the equivalent critical nucleation radius, Ω is the system molar volume (the molar volume is assumed to be the same in both the matrix and precipitate phases) a is the lattice parameter of the matrix, c_{xi} is the concentration of component i in either the precipitate ($x = k$) or ($x=0$) the matrix, s is the number of components in the system and D_{0i} is the bulk diffusion coefficient of component i in the matrix. The equivalent radius corresponds to a radius of a sphere with the same volume as that of the model precipitate. The bulk diffusion coefficient is used here as the microstructure is assumed to be homogeneous.

$$\beta^* = \frac{4\pi\rho^{*2}}{a^4\Omega} \left(\sum_{i=1}^s \frac{c_{0i}D_{0i}}{(c_{ki} - c_{0i})^2} \right) \quad (4)$$

Uniquely in the present model, the precipitate equivalent critical stable radius is calculated according to modified SFFK Equations which allow for a more complete dependence on the precipitate aspect ratio and, by extension, the misfit strain between the matrix and precipitate and also their elastic contrast; rather than the simple linear relationships defined in classical regimes, the value of ρ^* now equates to the maximum value of Equation 5 with respect to ρ . Here, ΔG represents the change in the Gibbs free energy of the system, the symbol λ_k corresponds to the precipitate-matrix misfit strain energy, ΔG_v is the thermodynamic driving force for precipitation, α_k is the precipitate aspect ratio calculated as the ratio of the precipitate major and minor axis lengths, ζ_k^E and ζ_k^M are the interfacial energies on the precipitate ends and mantle (defined below) respectively, m is the total number of precipitates and ξ_k is an as yet undefined term which the authors will refer to as the

dimensional ratio (the origin of term is explained below).

$$\Delta G = \sum_{k=1}^m \frac{4\pi\rho_k^{*3}}{3} (\lambda_k(\alpha_k) + \Delta G_v) + \sum_{k=1}^m 4\pi\rho_k^{*2} \frac{\xi_k^2}{8} \left(\zeta_k^E(\alpha_k) + 2\alpha_k \zeta_k^M(\alpha_k) \right) \quad (5)$$

Since precipitation is assumed to be homogeneous in this study, the number of sites for γ'' nucleation N is given by the quantity of atoms that could possibly form a precipitate remaining in the matrix *i.e.* those which could constitute one of the elemental constituents of γ'' precipitates but are not already locked up in the phase.

2.2. Precipitate Geometry

γ'' precipitates present with an oblate spheroidal shape with the contrast between the lengths of the major and minor axes becoming more pronounced as the particles grow viz. the aspect ratio experiences a significant decrease with increasing major radius [27]. Fully describing the curvature of the oblate spheroidal geometry and the implications this has for the interfacial energy is a severely non-trivial exercise and, moreover, the implementation of any such description is likely to lead to calculation times which are too long for most practical applications. Consequently, Svoboda *et al.* [14] include a far simpler adaptation in their SFFK model whereby biaxial precipitates such as needles and plates are modelled as cylinders.

The dimensions of the real precipitate are related to that of the cylinder such that they both have the same volume and aspect ratio. This is described mathematically by Equation 6 where A_k is the major axis of the real ellipsoid and B_k is the diameter of the cylinder. Replacing the axis with their values in terms of the equivalent radius defines the dimensional ratio ξ_k .

$$B_k = \sqrt{\frac{4}{3}} A_k = \xi_k \rho_k \quad (6)$$

2.3. Precipitate Evolution

The evolution of nucleated precipitates in the model takes place concomitantly with respect to radius and aspect ratio. Through inserting dependencies on both misfit strain (and therefore elastic contrast) and aspect ratio into the Equations of Svoboda *et al.* [12] for a system in which the interfacial mobility is unrestricted, the rate of change of the equivalent radius for a given precipitate (class) is now calculated in the present model according to Equation 7 where R is the ideal gas constant and O_k^1 is a factor derived from the equation governing the dissipation of the Gibbs energy in the system matrix which accounts for the cylindrical precipitate shape. Similarly the rate of aspect ratio change is defined according to Equation 8 where O_k^3 is another factor which accounts for precipitate shape but with different magnitude to O_k^{11} .

$$\dot{\rho}_k = - \left(\frac{\xi_k^2}{4\rho_k} \left(\zeta_k^E + 2\alpha_k \zeta_k^M \right) + \lambda_k(\alpha_k) + \Delta G_v + \frac{\rho_k}{3} \frac{d\lambda}{d\rho} + \frac{\xi_k^2}{8} \left(\frac{d\zeta_k^E}{d\rho} + \frac{d\zeta_k^M}{d\rho} \right) - \frac{\xi_k^2}{12\alpha_k} \frac{d\alpha}{d\rho} \left(\zeta_k^E - \alpha_k \zeta_k^M \right) \right) \cdot \left[\rho_k R T O_k^1 \sum_{i=1}^n \frac{(c_{ki} - c_{0i})^2}{c_{0i} D_{0i}} \right]^{-1} \quad (7)$$

$$\dot{\alpha}_k = - \left(\frac{\rho}{3} \frac{d\lambda}{d\alpha} - \frac{\xi_k^2}{12\alpha_k} \left(\zeta_k^E - \alpha_k \zeta_k^M \right) + \frac{\xi_k^2}{8} \left(\frac{d\zeta_k^E}{d\alpha} + \frac{d\zeta_k^M}{d\alpha} \right) \right) \left[\rho_k^3 R T O_k^3 \sum_{i=1}^n \frac{(c_{ki} - c_{0i})^2}{c_{0i} D_{0i} \alpha_k^2} \right]^{-1} \quad (8)$$

In addition to describing growth and aspect ratio change of an individual class, Equations 7 and 8 also allow for the concomitant growth and coarsening of new and existing precipitates/precipitate classes as the system evolves. As precipitation proceeds, the decreasing supersaturation in the matrix is calculated via a continuity equation shown in Equation 9

¹The equation including O_k^2 derived by Svoboda *et al.* is omitted here due to the condition imposed in this research of no diffusion taking place inside the precipitate

where N_i corresponds to the total quantity of element i in the system. Once calculated, the supersaturation value is in turn used to calculate the thermodynamic driving force for precipitate nucleation and growth ΔG_v .

$$c_{0i} = N_i - \sum_{k=1}^m \frac{4\pi\rho_{ki}^3}{3} \left[\Omega \sum_{i=1}^n \left(N_i - \sum_{k=1}^m \frac{4\pi\rho_{ki}^3}{3} \right) \right]^{-1} \quad (9)$$

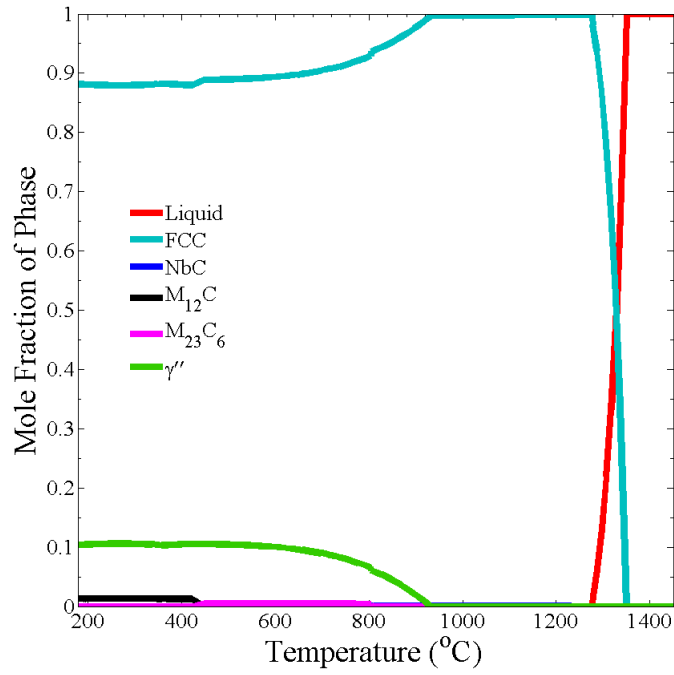
3. Literature Model Inputs

60 The aforementioned modifications made to the SFFK model swells the number of required inputs due to the removal of approximations regarding the evolution of variable values. The thermodynamic driving force precipitation in Alloy 625, for instance, is calculated for the model here through the use of the software Thermocalc (*i.e.* the CALPHAD method) employing the Ni-based Superalloys database version 7.0 (TCNI7) [28]; the stable phase trend
65 with temperature, as well as the composition of the γ'' predicted using this methodology for a sample of Alloy 625 with the composition defined in Table 1 is shown in Figure 2. Using these equilibrium predictions for the system, driving forces are updated during the calculation in accordance with the concentrations outputted by the continuity Equation.

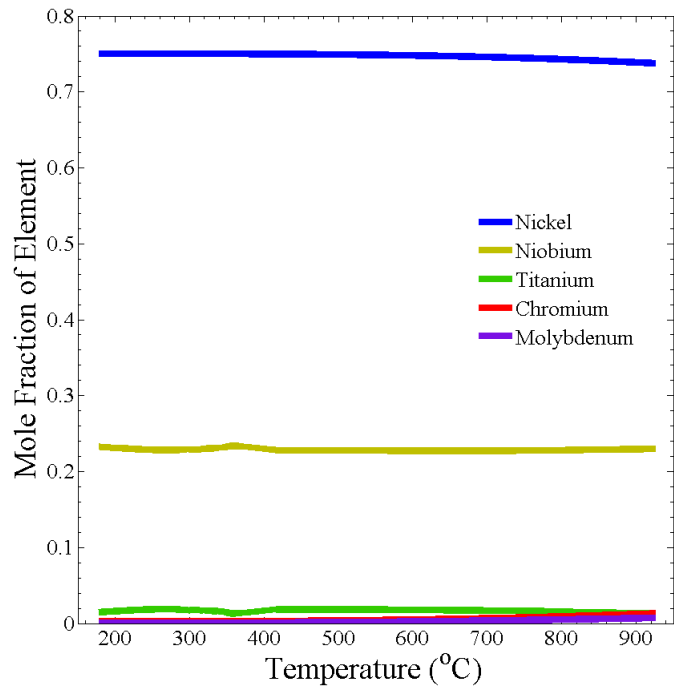
Table 1: Composition of Alloy 625 material used for simulation. The index * signifies fraction calculated from balance.

Element	Ni	Cr	Fe	Mo	Nb	C	Mn	Si	P	S	Al	Ti
wt%	62.0*	21.74	2.87	8.58	3.80	0.021	0.20	0.23	< 0.01	0.003	0.12	0.16

Another such input to the calculations is that of the elastic constants of both the precipitate and matrix phase. Unfortunately, the data reported in the literature for γ'' is quite
70 limited in terms of its temperature range [29] and therefore extrapolation, through mapping to calculations made for pure nickel over a wide temperature range by Luo *et al.* [30], is used



(a)



(b)

Figure 2: a) Molar phase composition of Alloy 625 and b) elemental composition of γ'' , both as a function of temperature. Data calculated using TCNI7 database via the CALPHAD method.

instead. Calibrating this trend to the data in the literature calculated by Connétable *et al.* [29] at zero kelvin yields the behaviour for the elastic constants shown in Figure 3; data used for the matrix phase corresponds to that measured for a piece of solution treated Alloy 625 material by the Special Metals Corporation [31].

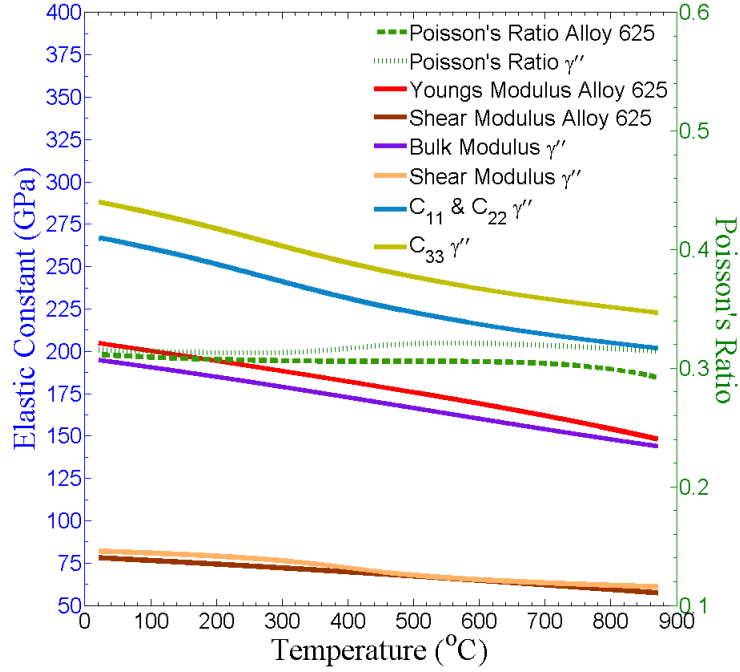


Figure 3: Inferred trends for Alloy 625 and γ'' elastic constant values with temperature utilised in the model presented in this paper. Owing to its comparatively stable behaviour, for simplicity the value for the Poisson's ratio is assumed in the model to be 0.3 always

In the absence of values for the diffusion coefficients within Alloy 625 being detailed in the literature, the data determined for diffusion of each of the constituent atoms forming the γ'' phase inside a nickel binary diffusion couple is utilised instead [32, 33, 34]. It should be noted that these coefficients are for bulk diffusion only due to the assumed homogeneity of the microstructure.

4. Experimental Inputs

4.1. Interfacial Energy

The elimination of symmetry caused by the introduction of separate interfacial energies for the precipitate cylinder mantle and ends means that the interfacial energies of the cylindrical precipitate can only be evaluated (via rearrangement of Equation 8) through calibrating them to an experimentally observed aspect ratio change rate. Accordingly, data for the evolution of γ'' precipitates was obtained from TEM analysis of thin foil specimens of aged Alloy 625 material with the composition listed in Table 1.

Samples were first solution-annealed at 1150°C for 30 minutes (following Shankar *et al.* [1]) before being aged at 650°C for periods of 100, 200, and 1000 hours, with foils prepared using the conventional twin-jet electropolishing techniques in an electrolyte of 20% HClO₄ 80% CH₃OH at -33°C. Subsequent characterisation of the foils using an FEI Tecnai T20 200 kV analytical transmission electron microscope produced [001]-oriented centred dark-field TEM images, such as those shown in Figure 4, from which the precipitate statistics were measured. The three [001] variants of the γ'' precipitates are evident in figure 4c.

4.2. Misfit Strain

Whilst Sarkar *et al.* [35] have made measurements of the lattice parameters (and *ipso facto* the misfit strain) of γ'' in Alloy 625, flaws in their deconvolution based x-ray method pertaining to it being performed on *in situ* precipitates mean their data are not appropriate for this model. In contrast, the ageing conditions and methodology employed by Slama *et al.* [36] in Alloy 718 (a related derivative alloy) are applicable and, therefore, values extrapolated (to 650°C) from these results were utilised here for calculation of the precipitate-matrix misfit strain tensor ϵ_{ij} as per Equation 10 [37]. The evolution of the misfit strain with respect to aspect ratio rather than time is achieved through a matching of the corresponding statistical

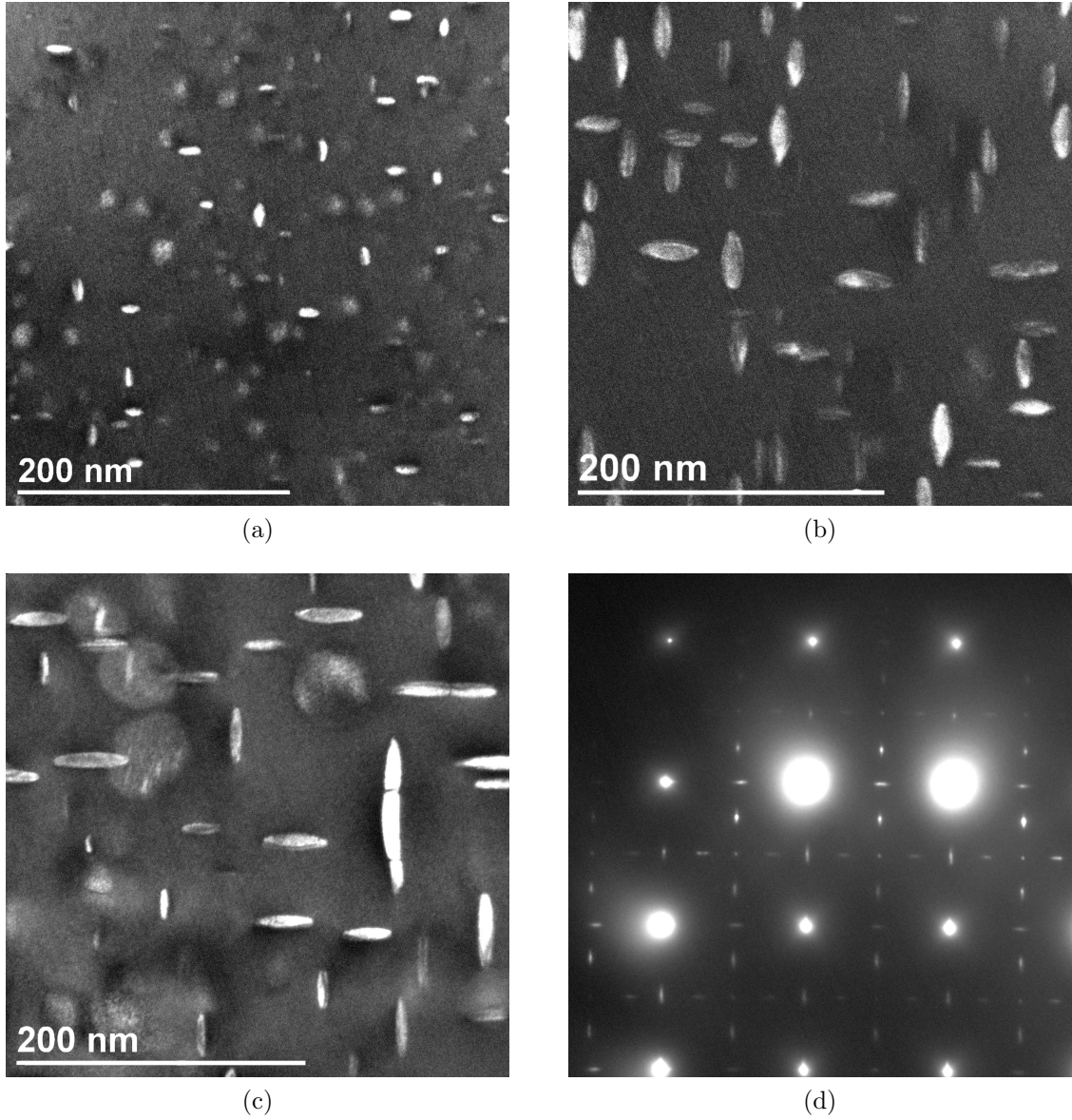


Figure 4: [001]-orientated dark field TEM images of γ'' precipitates in material aged at 650°C for a) 100, b) 200 and c) 1000 hours. d) [001] selected area diffraction pattern.

average values at the relevant times.

$$\epsilon_{ij} = \begin{pmatrix} \frac{a_{\gamma''} - a_{\gamma}}{a_{\gamma}} & 0 & 0 \\ 0 & \frac{a_{\gamma''} - a_{\gamma}}{a_{\gamma}} & 0 \\ 0 & 0 & \frac{\frac{c_{\gamma''}}{2} - a_{\gamma}}{a_{\gamma}} \end{pmatrix} \quad (10)$$

Following Cozar [38], the crystallographic alignment of the γ'' phase in the γ matrix dictates that the value of the components $\epsilon_{11}/\epsilon_{22}$ and ϵ_{33} correspond to the misfit strains of the cylinder mantle and ends respectively. As evidenced by Figure 5, however, the uncertainties in the measurements of Slama *et al.* allow for a wide range of possible fits meaning it is necessary to identify the appropriate trend for each through an iterative method; the trends presented for both stains in Figure 5 correspond to those where an appropriate final output for the model is achieved.

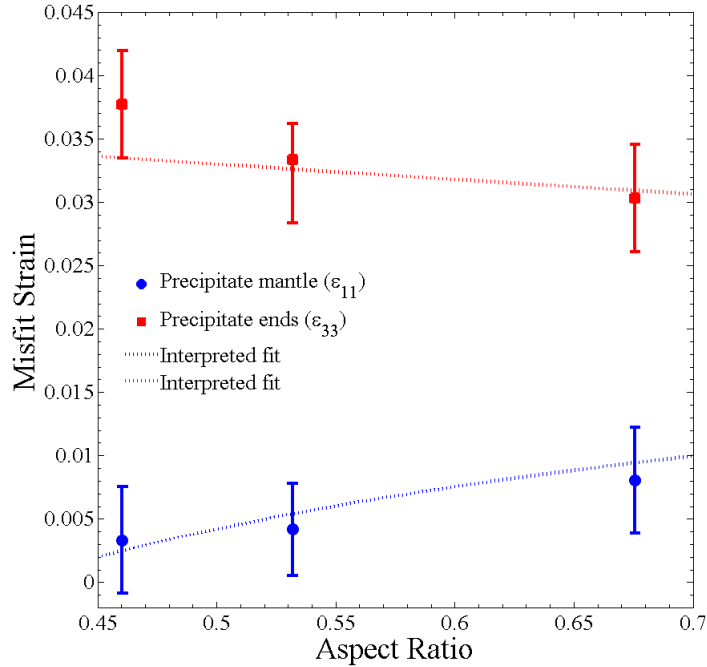


Figure 5: Misfit strain values calculated via Equation 10 using the lattice parameter values measured by Sarkar *et al.* [35] along with their interpreted hyperbolic fits.

Hagel *et al.* [39] suggested that a fully coherent interface can only be obtained if the value
105 of misfit strain at the interface is less than 1%. Correspondingly, analysis of the range of
values for ϵ_{11} over all aspect ratios yields the conclusion that the cylinder mantle maintains
a coherent boundary throughout the precipitate's evolution. In contrast, at the precipitate
ends, as indicated by ϵ_{33} , the interface is rather more incoherent at the start of precipitation
and quickly deteriorates. This result is important as it allows for the resolution of the
110 mathematical impasse of the determination of separate values for ζ^E and ζ^M by allowing
the reasonable assumption of an ideally coherent mantle-matrix interface (*i.e.* $\zeta^M = 0$ J).

4.3. $d\alpha/d\rho$

The mathematical relationship describing the average trend of precipitate aspect ratio
with precipitate major radius, used to calculate the value of $d\alpha/d\rho$ when solving Equation
115 7 as the simulation proceeds, is determined from fitting a hyperbolic decay to statistics of
all of the individually measured precipitates as per Figure 6.

5. Results and Discussion

In order generate an appropriate comparison, the simulation results correspond to an
Alloy 625 system 1 mole in size, with a composition identical to that detailed in Table 1
120 aged at 650°C. Utilising these values the magnitude of the system molar volume Ω is chosen
such that $\rho^* = 1.00$ nm but the actual value for the critical radius is actually enhanced
by 1% (to 1.01nm) in the model to ensure stability for nucleating particles. A result of
the selection of this magnitude for ρ^* , is the creation of a time shift in calculated data of
precipitates with a magnitude (determined from the aspect ratio evolution data) of 32.73
125 hours, therefore each of the modelled data sets presented are necessarily displaced with
respect to time by a corresponding magnitude. Beginning with a magnitude of 0.1 seconds,

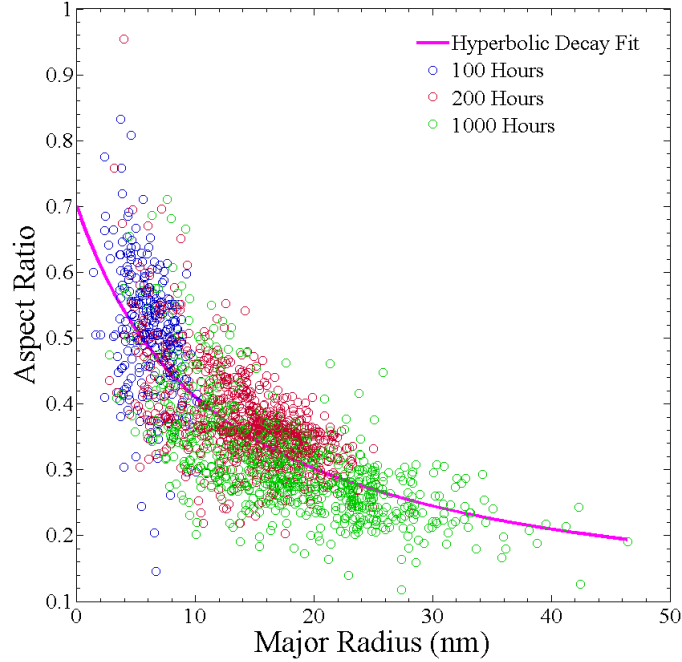


Figure 6: Aspect ratio and major radius for γ'' precipitates formed at 650°C after ageing for 100, 200 and 1000 hours.

the time step implemented in the simulation increased by a magnitude of 1% per iteration subject to both restrictions on parameter changes between steps (leading to a time step decrease if exceeded) and a maximum magnitude of 3600s to retain detail. Finally, in order to ensure the correct calculation of the precipitate statistics each of the datasets presented here relate to the distribution density evaluated using the procedure of Perez *et al.* [40], rather than the raw classes as output by the model.

5.1. Aspect Ratio Distribution

Comparison of the experimental data fit with the average model data points shown in Figure 7 shows the model to correctly reproduce the calibration data, with almost perfect agreement with the experimental data fit achieved. Such a correlation between the fitted and average $\alpha(t)$ trends, whilst important, is obviously necessarily expected, however it is also worth noting the very narrow limit the spread of generated distributions. The occurrence of this latter phenomenon derives from the utilisation of the fitted $\alpha(t)$ trend for the calculation

140 of the interfacial energy of all the classes which forces all particles to principally follow this path. Clearly, the contrast between this mathematically-generated aspect ratio distribution and those indicated for the experimental data highlights a limitation of the model with respect to this variable. However, as average values (particularly precipitate size and number density) constitute the key statistics in calculating the impact of a precipitate distribution
 145 on the properties of Alloy 625 this limitation does not constitute a significant problem in the application of the model results.

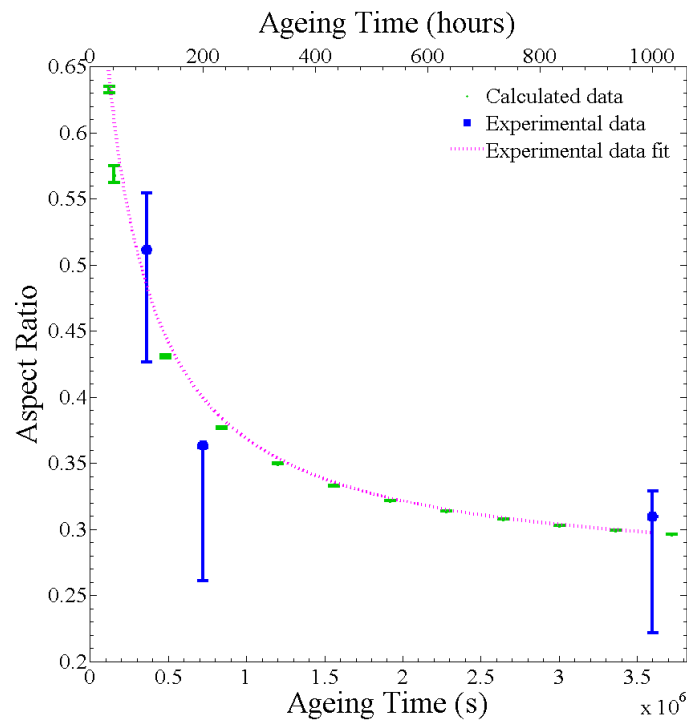


Figure 7: Aspect ratio distribution density trend calculated for γ'' precipitates in Alloy 625 when ageing at 650°C. The data points correspond to mean values with the error bars indicating the first and fourth quartiles of the distribution. Experimental data points and their hyperbolic which is input to the model are shown for comparison.

5.2. Particle Size Distribution

Inspection of Figure 8 yields the conclusion that a reasonable agreement between the model generated values and the nominal hyperbolic fit to the experimental data is obtained;
 150 the underestimation of approximately 1 nm at extended ageing times is consistent with

the raw experimental data. Furthermore, it can also be observed through comparison of the relative first and third quartiles of both the experimental and calculated distributions that the model is remarkably successful in replicating the shape of the distribution as well. This result is marked as it provides evidence that fixing the aspect ratio evolution has little
 155 detrimental impact on the more significant major radius statistics.

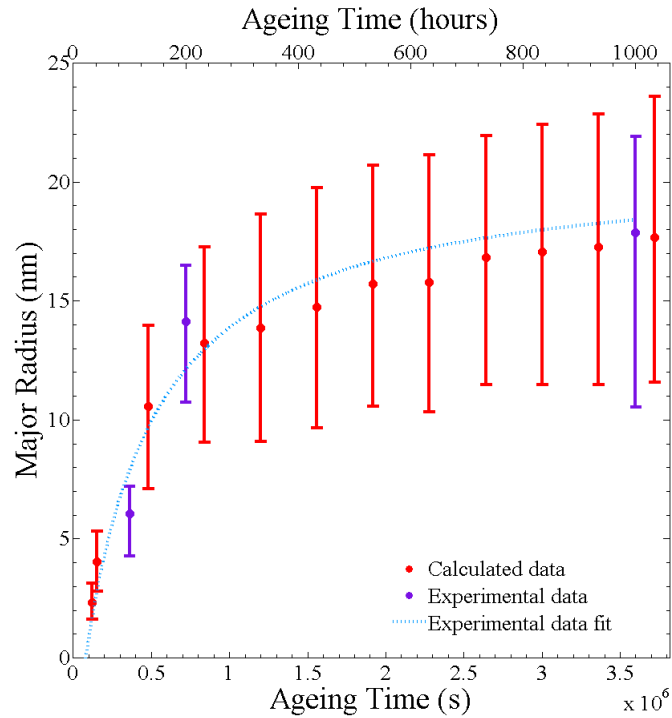


Figure 8: Particle size distribution density trend calculated for γ'' precipitates in Alloy 625 aged at 650°C. The data points correspond to mean values with the error bars indicating the first and fourth quartiles of the distribution. Experimental data points and their hyperbolic which is input to the model are shown for comparison.

5.3. Particle Number Density

Before an accurate comparison with experimental data can be made, it is first necessary to adjust the model dataset such that it corresponds to a system with a molar volume equivalent to the relative matrix value used in the calculation of the experimental statistics. In this case derived from the measurements of Sarkar *et al.* [35]). Subsequent to such an
 160 operation, Figure 9 highlights the fact that an extremely good replication is achieved by

the model albeit with an increasingly small divergence with time. The existence of such a separation is not surprising owing to both the lack of competing precipitate phases for niobium (such as carbides) in the model and the slightly smaller width of the distributions in Figure 8. A smaller distribution width necessitates a higher number density must be created to generate the same precipitate volume fraction as that observed in the real system.

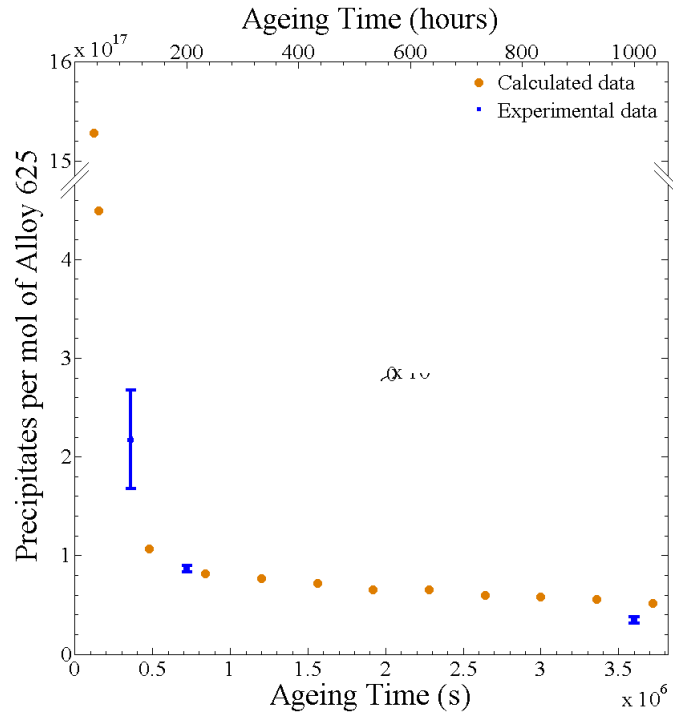


Figure 9: Calculated and experimentally observed number density evolution for γ'' particles

5.4. Interfacial Energy

Rather than a true interfacial energy as previously defined, it turns out that the actual value of ζ_k^E in the model is that of an effective energy accounting for both the interfacial energy and the effect of changing coherency on the misfit strain. In other words, as the calculation of misfit strain is based principally on the lattices of precipitate and matrix always retaining full coherency and because the model does not include an appropriate reduction for the strain which accompanies the transition to a semi-coherent or fully incoherent interface in the real system, the value of ζ_k^E must change to compensate. The mathematical contribution

of this phenomenon to ζ_k^E can be derived from the free energy equation (Equation 5) as per Equation 11, where Z_k^E corresponds to the actual interfacial which should be attributed to the ends of the cylindrical precipitates constructed in the model and Λ_k is the contribution from the reduction in misfit strain.

$$\zeta_k^E = Z_k^E + \frac{8\rho_k}{3\xi_k^2}\Lambda_k^E \quad (11)$$

Whilst non-trivial, successful deconvolution of the two contributions to the output ζ_k^E values can be achieved under the condition of a fixed U value (as defined in Equation 12) through consideration of their impact on the evolution of the interfacial energy at constant aspect ratio: $\zeta_k^E(\rho_{\alpha=\text{constant}})$ happens to be well fitted by a second order polynomial, meaning that the reasonable assumption that $Z_k^E(\rho_{\alpha=\text{constant}})$ shares the same form generates the relations in Equation 13. Consequently, comparison of the polynomial relations detailed in Equation 14, calculated from the evaluation of the coefficients A_ζ , B_ζ and C_ζ over all aspect ratios, indicates the value of B_ζ should also follow a second order polynomial if the influence of the factor $8\Lambda_k[3\xi_k^2]^{-1}$ is removed. Therefore, as the degeneration of the precipitate-matrix interface should be at a minimum at the start of precipitate nucleation and growth, the mathematical description of B_Z and (from its remainder) $8\Lambda_k[3\xi_k^2]^{-1}$ can be evaluated from B_ζ by fitting a second order polynomial to data points corresponding to high aspect ratios.

$$U = \sum_{i=1}^s \frac{(c_{ki} - c_{0i})^2}{c_{0i}D_{0i}} \quad (12)$$

$$\begin{aligned} \zeta_k^E &= A_\zeta(\alpha_k)\rho_k^2 + B_\zeta(\alpha_k)\rho_k + C_\zeta(\alpha_k) \\ A_\zeta\rho_k^2 + B_\zeta\rho_k + C_\zeta &= A_Z\rho_k^2 + B_Z\rho_k + C_Z + \frac{8\rho_k}{3\xi_k^2}\Lambda_k^E \end{aligned} \quad (13)$$

$$A_\zeta = A_Z \quad B_\zeta = B_Z + \frac{8}{3\xi_k^2}\Lambda_k^E \quad C_\zeta = C_Z$$

$$\begin{aligned}
A_\zeta &= A_\zeta^1(U)\alpha_k^2 + A_\zeta^2(U)\alpha_k + A_\zeta^3(U) \\
B_\zeta &= B_\zeta^1(U)\alpha_k^7 + B_\zeta^2(U)\alpha_k^6 + B_\zeta^3(U)\alpha_k^5 + B_\zeta^4(U)\alpha_k^4 + B_\zeta^5(U)\alpha_k^3 + B_\zeta^6(U)\alpha_k^2 + B_\zeta^7(U)\alpha_k + B_\zeta^8(U) \\
C_\zeta &= C_\zeta^1(U)\alpha_k^2 + C_\zeta^2(U)\alpha_k + C_\zeta^3(U)
\end{aligned} \tag{14}$$

Using this methodology over a range of U values the coefficients in Equation 14 are defined according to the surfaces in Figure 10. The resultant separate/deconvoluted contributions to the ζ_k^E distribution (Figure 11) provide evidence of a concomitant increase in interfacial energy and reduction in misfit strain energy evolution consistent with precipitates becoming increasingly incoherent with the matrix as they grow.

Analysis of the evolution of the contributions to the mean interfacial energy when averaged over the entire particle surface (*i.e.* ζ_k) with the mean aspect ratio as presented in Figure 12 shows the data to be consistent with the inclusion theory of Eshelby [41, 42]. That is to say, a decrease in the aspect ratio is accompanied by both an increase in the interfacial energy and a drop in the elastic energy as evidenced by the trends of Z_k^E and the misfit strain energy reduction ($8\rho_k\Lambda_k^E[3\xi_k^2]^{-1}$) respectively. Furthermore, extrapolation from the data series shows conformity for the asymptote in the misfit reduction with the definition of γ'' -matrix incoherency made by other authors in Alloy 718 [27, 38, 36]; typically an average major radius of around 50 nm (*cf.* Figure 8) and aspect ratio of <0.2 .

The most appropriate comparison of the dynamic interfacial energy value produced by the model with those detailed in the literature can seemingly be made by identifying the value for Z_k for an average precipitate at the corresponding values of the misfit strains ϵ_{11} and ϵ_{33} . Unfortunately as shown in Table 2, however, such an approach is fundamentally flawed due to the large disparity (unaccounted for simply by temperature differences) in the relative magnitude of the two variables *e.g.* when $\epsilon_{33} = 2.86 \times 10^{-2}$ Devaux *et al.* state

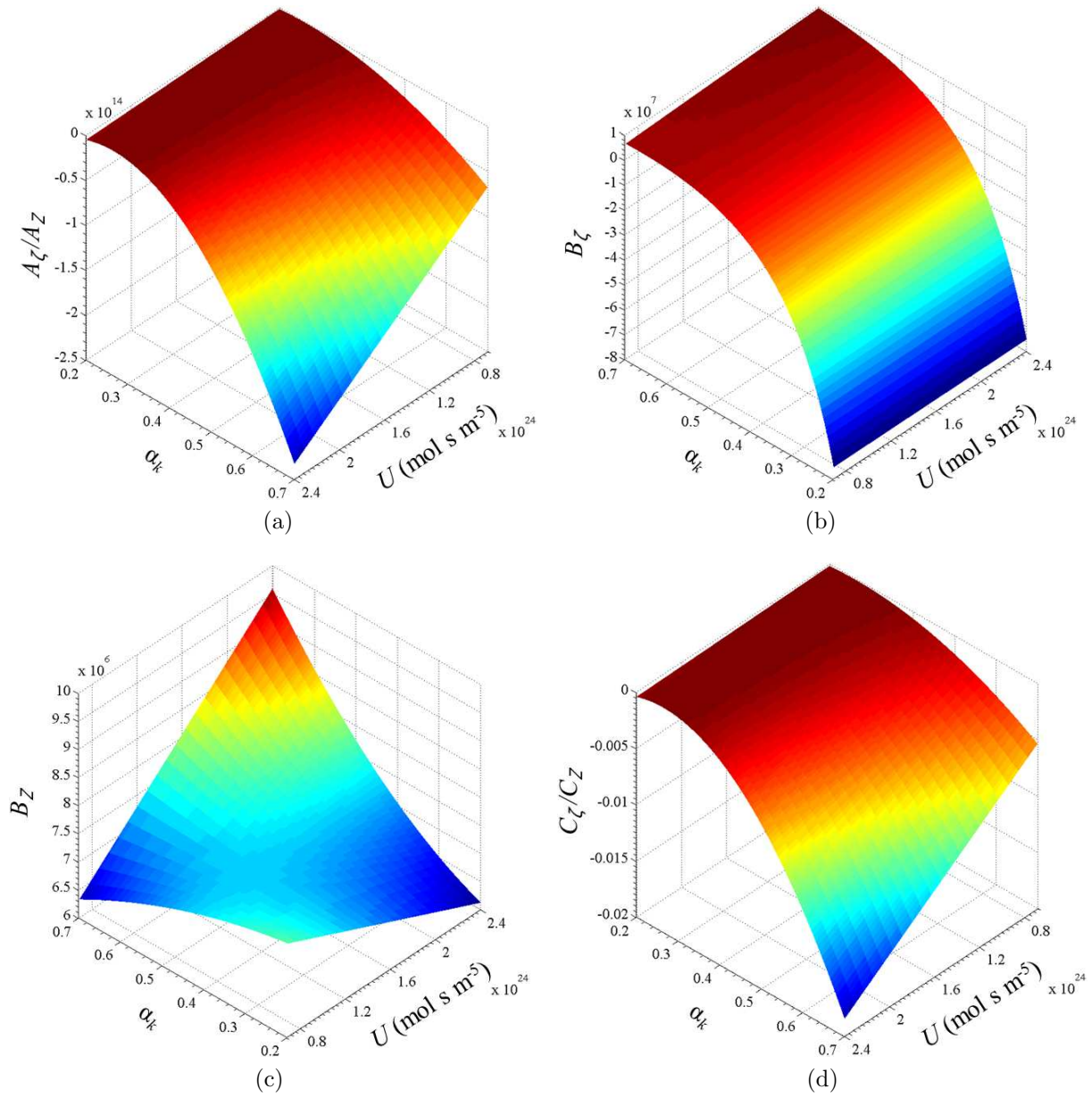


Figure 10: Contours for the coefficients in Equations 13 and 14 a) A_ζ , b) B_ζ , c) B_Z and c) C_ζ .

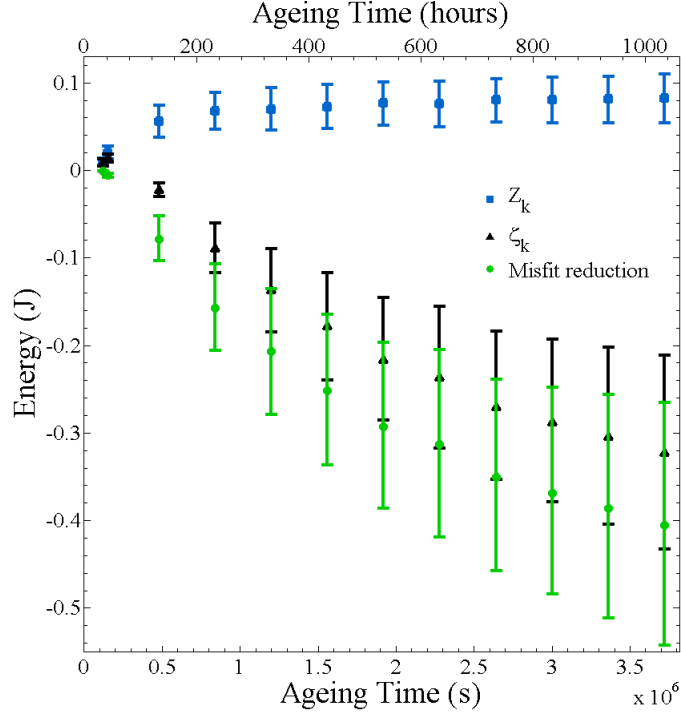


Figure 11: ζ_k^E evolution for γ'' particles together with its deconvoluted contributions from ζ_k^E and the reduction in misfit strain energy ($8\rho_k\Lambda_k^E[3\zeta_k^2]^{-1}$). Data points correspond to average values and the error bars to the first and third quartiles of the interfacial energy distribution.

$\epsilon_{11} = 6.67 \times 10^{-3}$ whereas the fits in Figure 5 show $\epsilon_{11} = 2.2 \times 10^{-3}$.

Table 2: Literature values for the interfacial energy and misfit strain between γ'' precipitates and the matrix of nickel based alloys.

	System	Interfacial Energy (mJ)	$\epsilon_{11}(\times 10^{-3})$	$\epsilon_{33}(\times 10^{-2})$
Cozar <i>et al.</i> [38]	Fe 30.8-Ni	145	9.4 ± 0.3	3.72 ± 0.06
	9.1-Ta	185	7.0	3.46
Devaux <i>et al.</i> [27]	Alloy 718	97 ± 17	6.67	2.86
Slama <i>et al.</i> [36] (750°C, 4h)	Alloy 718	—	8.9 ± 3.1	2.96 ± 0.30
This Study (Average Precipitate)	Alloy 625	$0 \rightarrow 51.84$	$\rightarrow -23.5$	$\rightarrow 3.7$

The cause for this significant disagreement with the misfit strains and, ultimately, the

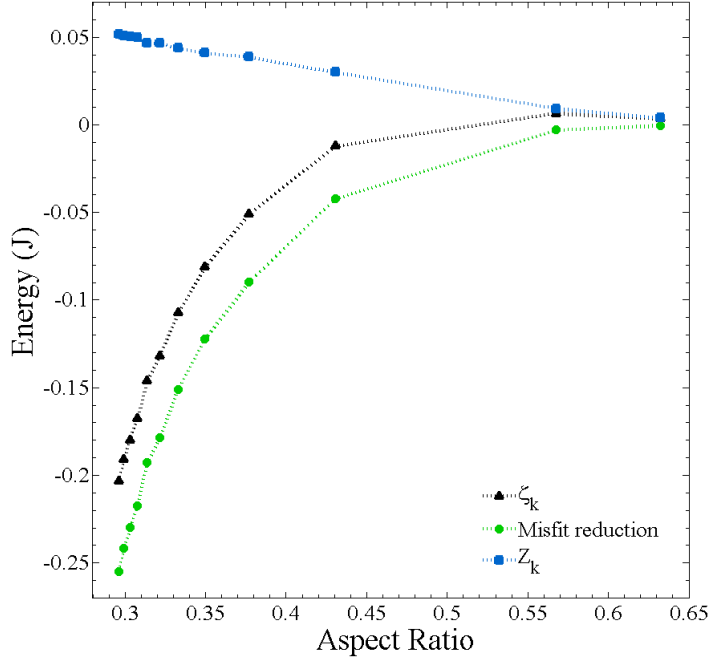


Figure 12: Evolution of the average values ζ_k , Z_k and $8\rho_k\Lambda_k[3\xi_k^2]^{-1}$ with average aspect ratio calculated from their relative distributions.

190 interfacial energies listed by both Cozar *et al.* [38] and Devaux *et al.* almost certainly arises due to the different systems each is associated with and the assumptions made in their derivation: With respect to the results of Cozar *et al.*, whilst the authors note that the value for the interfacial energy is probably enhanced due to the loss in coherency between the γ'' precipitates in the majority iron matrix as opposed to a majority nickel one, it is far
 195 more likely that it is the incorporation of tantalum rather than niobium leading to much a longer $c_{\gamma''}$ lattice parameter (whilst leaving a_γ and $a_{\gamma''}$ relatively unchanged) which is responsible for incompatibility with the model Z_k and ϵ_{33} values. In contrast, although the values calculated by Devaux *et al.* [27] are apparently principally based on values for the lattice parameters of niobium containing γ'' measured by Wagner *et al.* [43] at 750°C,
 200 comparison with those of Slama *et al.* [36] and (for ϵ_{11}) Cozar *et al.* [38] in Table 2 suggest they represent a severe underestimate owing to too large of a value being utilised for a_γ . Assuming all other factors in the free energy balance equation are approximately equivalent

to those used in the model, the result of this underestimation will be a compensatory over estimation of the interfacial energy Z_k *cf.* for an average model precipitate at 650°C when
205 $\epsilon_{11} = 6.67 \times 10^{-3}$, $\alpha = 0.57$ and $Z_k = 9.22$ mJ.

In the light of the problems discussed for the literature interfacial energy values calculated for γ'' precipitates, one can only conclude that their conformity with respect to the order of magnitude evolution of the modelled data shows broad agreement is achieved. Similarly, owing to their different structure, composition, range and probable analogous problems with
210 their applicability relating to their derivation, alternative comparison to values calculated for γ' precipitates in Ni-Ti and Ni-Al systems such as those reassessed over many years using the LSW theory by Ardell [44, 45, 46] of *ca.* 6.6-94 mJ also yields only a successful order of magnitude check.

6. Conclusions

215 Drawing on many mathematical relations described in the literature, a modified SFFK model for γ'' precipitates in Alloy 625 has been created which produces statistics for precipitate number density, aspect ratio, major radius and interfacial energy. Some minor disparity with experimental values gathered both in this study and described in the literature is evidenced as a consequence of assumptions made both in their derivation and by the model.
220 However, based on the degree of precision desired for the appropriate calculation of mechanical properties such as material hardness for material manufacture and service performance the model data can be considered as an appropriate reproduction. To the author's knowledge, this study is the first instance of such statistics being calculated for γ'' precipitates and also for the production of a dynamic value of the interfacial energy in a class type computa-
225 tion. Ultimately, the outlined methodology derived with respect to γ'' precipitates can allow for the calculation of similar statistics in many other spherical and spheroidal (including needle-shaped) precipitate systems (making appropriate shape corrections consistent with

Svoboda *et al.* [14]).

Acknowledgements

230 This work was funded by the Engineering and Physical Sciences Research Council under
the auspices of the Nuclear FiRST doctoral training centre based at The University of
Sheffield and The University of Manchester.

References

- [1] V. Shankar, K. Bhanu Sankara Rao, S. Mannan, Microstructure and mechanical properties of Inconel
235 625 superalloy, *Journal of Nuclear Materials* 288 (2-3) (2001) 222–232.
- [2] J. Chakravartty, J. Singh, M. Sundararaman, Microstructural and mechanical properties of service
exposed Alloy 625 ammonia cracker tube removed after 100 000h, *Materials Science and Technology*
28 (6) (2012) 702–710.
- [3] J. Crum, G. Smith, H. Flower, Resistance of Automotive Exhaust Flexible Coupling Alloys to Hot
240 Salt Attack, Stress Corrosion Cracking and High Temperature Embrittlement, SAE Technical Paper
1999-01-0372.
- [4] J. Rakowski, C. Stinner, M. Lipschutz, J. Montague, The Use and Performance of Wrought 625 Alloy
in Primary Surface Recuperators for Gas Turbine Engines, in: E. Loria (Ed.), *Proceedings of the
International Symposium on Superalloys 718, 625, 706 and Various Derivatives*, The Minerals, Metals
245 & Materials Society, Warrendale, PA, 2005, pp. 271–286.
- [5] D. Capitanescu, Alloy 625 weld overlays for offshore and onshore projects, in: E. Loria (Ed.), *Proceed-
ings of the International Symposium on Superalloys 718, 625 and Various Derivatives*, The Minerals,
Metals & Materials Society, Warrendale, PA, 1991, pp. 821–835.
- [6] M. Kutz, *Handbook of Materials Selection*, John Wiley & Sons, Inc., New York, NY, 2002.
- 250 [7] R. Bajaj, W. Mills, M. Lebo, B. Hyatt, M. Burke, Irradiation-assisted stress corrosion cracking of HTH
Alloy X-750 and Alloy 625, *The Minerals, Metals & Materials Society*, Breckenridge, CO, 1995, pp.
1093–1107.
- [8] J. Oblak, D. Paulonis, D. Duvall, Coherency strengthening in Ni base alloys hardened by D0₂₂ γ''
precipitates, *Metallurgical Transactions* 5 (1974) 143–153.

- 255 [9] J. Oblak, D. Duvall, D. Paulonis, An estimate of the strengthening arising from coherent, tetragonally-distorted particles, *Materials Science and Engineering* 13 (1) (1974) 51–56.
- [10] M. Jackson, R. Reed, Heat treatment of Udimet 720Li: The effect of microstructure on properties, *Materials Science and Engineering A* 259 (1) (1999) 85–97.
- [11] E. L. Raymond, D. Wells, Effects of aluminum content and heat treatment on gamma prime structure and yield strength of Inconel nickel-chromium Alloy 706, in: *Superalloys 1972 (Proceedings of the Second International Symposium on Superalloys)*, The Minerals, Metals & Materials Society, Warrendale, PA, 1972, pp. N1–N21.
- 260 [12] J. Svoboda, F. Fischer, P. Fratzl, E. Kozeschnik, Modelling of kinetics in multi-component multi-phase systems with spherical precipitates I: Theory, *Materials Science and Engineering A* 385 (1-2) (2004) 166–174.
- 265 [13] E. Kozeschnik, J. Svoboda, F. Fischer, Shape factors in modeling of precipitation, *Materials Science and Engineering A* 441 (1-2) (2006) 68–72.
- [14] J. Svoboda, F. Fischer, P. Mayrhofer, A model for evolution of shape changing precipitates in multi-component systems, *Acta Materialia* 56 (17) (2008) 4896–4904.
- 270 [15] R. Kampmann, R. Wagner, Kinetics of precipitation in metastable binary alloys - theory and application to Cu-1.9at% Ti and Ni-14at% Al., in: P. Hassen (Ed.), *Decomposition of alloys, the early stages: proceedings of the 2nd Acta-Scripta Metallurgica Conference.*, Oxford, UK, 1984, pp. 91–103.
- [16] R. Wagner, R. Kampmann, P. Voorhees, *Homogeneous Second-Phase Precipitation*, Wiley-VCH Verlag GmbH & Co. KGaA, 2005, pp. 309–407.
- 275 [17] E. Kozeschnik, J. Svoboda, P. Fratzl, F. Fischer, Modelling of kinetics in multi-component multi-phase systems with spherical precipitates II: Numerical solution and application, *Materials Science and Engineering A* 385 (1-2) (2004) 157–165.
- [18] A. Deschamps, M. Perez, Mesoscopic modelling of precipitation: A tool for extracting physical parameters of phase transformations in metallic alloys [modlisation mesoscopique de la precipitation: Un outil pour extraire les paramtres physiques des transformations de phase dans des alliages mtalliques], *Comptes Rendus Physique* 11 (3-4) (2010) 236–244.
- 280 [19] K. Janssens, D. Raabe, E. Kozeschnik, M. Miodownik, B. Nestler, *Computational Materials Engineering: An Introduction to Microstructure Evolution*, Elsevier Science, London, UK, 2010.
- [20] L. Ratke, P. Voorhees, *Growth and Coarsening: Ostwald Ripening in Material Processing*, *Engineering Materials*, Springer-Verlag, Berlin, Heidelberg, New York, 2002.
- 285

- [21] L. Onsager, S. MacHlup, Fluctuations and irreversible processes, *Physical Review* 91 (6) (1953) 1505–1512.
- [22] K. Russell, Nucleation in solids: The induction and steady state effects, *Advances in Colloid and Interface Science* 13 (3-4) (1980) 205–318.
- 290 [23] J. Zeldovich, Theory of new phase formation: cavitation, *Acta Physicochimica* 18 (1943) 1–22.
- [24] J. Feder, K. Russell, J. Lothe, G. Pound, Homogeneous nucleation and growth of droplets in vapours, *Advances in Physics* 15 (57) (1966) 111–178.
- [25] P. Shewmon, *Diffusion in Solids*, 2nd Edition, Wiley, Chichester, UK, 1989.
- [26] H. Mehrer, *Diffusion in Solids: Fundamentals, Methods, Materials, Diffusion-controlled Processes*, Springer series in solid-state sciences, Springer-Verlag, New York, NY, 2007.
- 295 [27] A. Devaux, L. Nazé, R. Molins, A. Pineau, A. Organista, J. Guédou, J. Uginet, P. Héritier, Gamma double prime precipitation kinetic in Alloy 718, *Materials Science and Engineering A* 486 (1-2) (2008) 117–122.
- [28] ThermoCalc, Thermo-Calc Software TCNI7 Ni-based Superalloys database version 7, Stockholm, Sweden.
- 300 [29] D. Connétable, M. Mathon, J. Lacaze, First principle energies of binary and ternary phases of the Fe-Nb-Ni-Cr system, *Calphad: Computer Coupling of Phase Diagrams and Thermochemistry* 35 (4) (2011) 588–593.
- [30] F. Luo, X.-R. Chen, L.-C. Cai, Q. Wu, Thermoelastic properties of nickel from molecular dynamic simulations, *Journal of Atomic and Molecular Sciences* 2 (1) (2011) 10–19.
- 305 [31] Special Metals Corporation, Inconel Alloy 625, <http://www.specialmetals.com/documents/Inconel%20alloy%20625.pdf>, (Last accessed 1 January 2016) (August 2013).
- [32] A. R. Wazzan, Lattice and grain boundary self-diffusion in nickel, *Journal of Applied Physics* 36 (11) (1965) 3596–3599.
- 310 [33] M. Karunaratne, D. Cox, R. Reed, Modelling of the microsegregation in CMSX-4 superalloy and its homogenisation during heat treatment, in: T. Pollock, R. Kissinger, K. Green, M. McLean, S. Olson, J. Schirra (Eds.), *Superalloys 2000 (Proceedings of the Ninth International Symposium on Superalloys)*, The Minerals, Metals & Materials Society, Warrendale, PA, 2000, pp. 263–272.
- [34] M. Karunaratne, R. Reed, Interdiffusion of niobium and molybdenum in nickel between 900 - 1300°C, *Defect and Diffusion Forum* 237-240 (PART 1) (2005) 420–425.
- 315 [35] A. Sarkar, P. Mukherjee, P. Barat, T. Jayakumar, S. Mahadevan, S. Rai, Lattice misfit measurement in

Inconel 625 by X-ray diffraction technique, *International Journal of Modern Physics B* 22 (23) (2008) 3977–3985.

- 320 [36] C. Slama, C. Servant, G. Cizeron, Aging of the inconel 718 alloy between 500 and 750°C, *Journal of Materials Research* 12 (9) (1997) 2298–2316.
- [37] R. Cozar, Etude de la precipitation des phases γ' (L_{12}) et γ'' ($D0_{22}$) dans des aciers austenitiques Fe-Ni-(Co)-Ta et des superalliages derives de l'Inconel 718. [Study of the precipitation of phases γ' (L_{12}) and γ'' ($D0_{22}$) in the austenitic steel Fe-Ni-(Co)-Ta and derivatives of the superalloy Inconel 718], Ph.D. thesis, Université de Nancy 1, Nancy, FR (1973).
- 325 [38] R. Cozar, A. Pineau, Influence of coherency strains on precipitate shape in a Fe-Ni-Ta alloy, *Scripta Metallurgica* 7 (8) (1973) 851 – 854.
- [39] W. C. Hagel, H. R. Beattie, *Precipitation Processes in Steels*, Percy Lund Humphries & Co. Ltd., London, UK, 1959, p. 98.
- [40] M. Perez, C. Sidoroff, A. Vincent, C. Esnouf, Microstructural evolution of martensitic 100Cr6 bearing steel during tempering: From thermoelectric power measurements to the prediction of dimensional changes, *Acta Materialia* 57 (11) (2009) 3170–3181.
- 330 [41] J. Eshelby, The determination of the elastic field of an ellipsoidal inclusion and related problems, *Proceedings of the Royal Society of London. Series A, Mathematical and Physical Sciences* 241 (1226) (1957) 376–396.
- 335 [42] J. Eshelby, The elastic field outside an ellipsoidal inclusion, *Proceedings of the Royal Society of London. Series A, Mathematical and Physical Sciences* 252 (1271) (1959) 561–569.
- [43] H. Wagner, A. Hall, *Physical Metallurgy of Alloy 718*, <http://www.dtic.mil/dtic/tr/fulltext/u2/466476.pdf> DMIC Report 217 (1965).
- [44] A. Ardell, The growth of gamma prime precipitates in aged Ni-Ti alloys, *Metallurgical and Materials Transactions B* 1 (2) (1970) 525–534.
- 340 [45] A. Ardell, Interfacial free energies and solute diffusivities from data on ostwald ripening, *Interface Science* 3 (2) (1995) 119–125.
- [46] A. Ardell, A1-L1₂ interfacial free energies from data on coarsening in five binary Ni alloys, informed by thermodynamic phase diagram assessments, *Journal of Materials Science* 46 (14) (2011) 4832–4849.